



Full Length Article

Exploring mechanical properties of Net Y: A molecular dynamics examination on the impact of defect density and temperature gradients under uniaxial tension

Mohsen Eghbalian^a, Mohammad Javad Hashemi^a, Amirhossein Nikparsa^a , Reza Ansari^{a,b,*}, Saeid Sahmani^{b,c,*}, Eligiusz Postek^d

^a Faculty of Mechanical Engineering, University of Guilan, P.O. Box 3756, Rasht, Iran

^b Department of Civil Engineering, School of Science and Technology, The University of Georgia, Tbilisi 0171, Georgia

^c School of Civil, Environmental, and Architectural Engineering, Korea University, Seoul 02841, Republic of Korea

^d Institute of Fundamental Technological Research, Polish Academy of Sciences, Pawińskiego 5B, 02-106 Warsaw, Poland

ARTICLE INFO

Keywords:

Carbon allotrope

Net Y

Molecular dynamics simulation

Mechanical properties

Defect density

ABSTRACT

After the synthetization of graphene, various carbon allotropes with remarkable applications have emerged in the material science. Net Y, closely related to Net C, is a novel carbon allotrope with exceptional properties. This study employs the molecular dynamics simulation to predict key mechanical characters of Net Y subjected to a uniaxial tension, including the failure strain as well as stress, Young's modulus, and strain energy. A detailed tension distribution analysis is provided to explore its mechanical behavior further. The numerical results reveal that the defect density and temperature gradients significantly influence the mechanical performance of Net Y. The nanosheet exhibits over twice the failure stress and 1.5 times the failure strain along with the X direction than the initial failure stress and strain observed along with the Y direction. Also, it is demonstrated that the ultimate failure stress as well as strain along with the Y direction are more significant due to a substantial failure region in the associated stress–strain path. Furthermore, it is observed that the Young's modulus declines consistently allocated to a higher defect density, decreasing by approximately 17 % via increasing the defect density from 0.5 % to 2 % along with the X direction. Moreover, the quantity of strain energy increases with the number of ribbons, reaching 1.58×10^{-26} eV and 3.99×10^{-26} eV along with the X and Y directions, respectively. The study also emphasizes the importance of defect location and structural stability through the tension distribution analysis.

1. Introduction

Carbon allotropes and carbon nanomaterials play a substantial role in the field of nanomaterials and nanoscience. Their exceptional mechanical, physical, and electronic properties make them promising candidates for increasing efficiency and contributing to the development of various industries over the past decades. Graphene exhibits excellent mechanical and physical properties and has various promising applications. Due to its extraordinary conductivity and high mechanical strength, it is used in flexible electronics, supercapacitors, and sensors [1–7]. Since the discovery of graphene, various carbon allotropes have been studied through different carbon atom hybridizations. The field of carbon allotropes research emphasizes their significance through key

applications. Fullerenes, graphite, nanotubes, nanoribbons, diamond, and nanowires are promising nanostructures introduced for their remarkable properties and high-potential applications. As a result, scientists have comprehensively studied their potential and behavior [8–19].

In addition, graphyne and graphdiyne are other 2D carbon nanomaterials that have been synthesized in recent years [20]. Due to the combination of sp-hybridized and sp²-hybridized carbon atoms following a specific periodic pattern, graphynes exhibit distinct structures and properties compared to other carbon allotropes, which consist solely of sp²-hybridized carbon atoms [21,22]. It is also worth mentioning that graphdiyne was the first among C-materials synthesized through wet chemistry under moderate conditions, comprising both sp²

* Corresponding authors.

E-mail addresses: r.ansari@guilan.ac.ir (R. Ansari), s.sahmani@ug.edu.ge (S. Sahmani).

<https://doi.org/10.1016/j.commsci.2025.114049>

Received 13 April 2025; Received in revised form 10 June 2025; Accepted 11 June 2025

Available online 14 June 2025

0927-0256/© 2025 Elsevier B.V. All rights reserved, including those for text and data mining, AI training, and similar technologies.

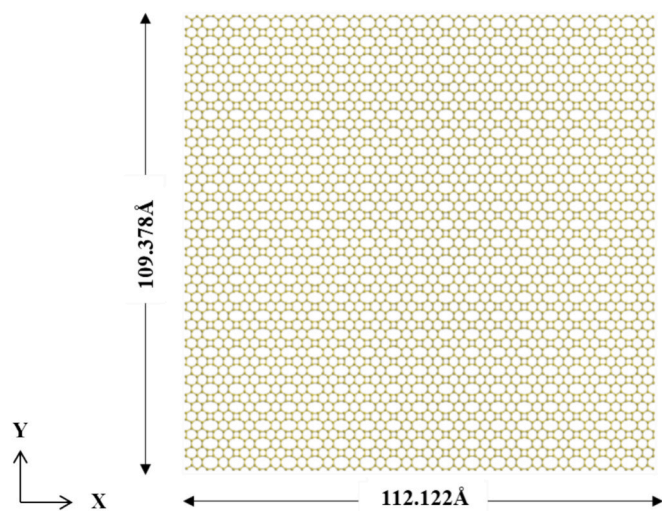


Fig. 1. Front view of the Net Y nanostructure.

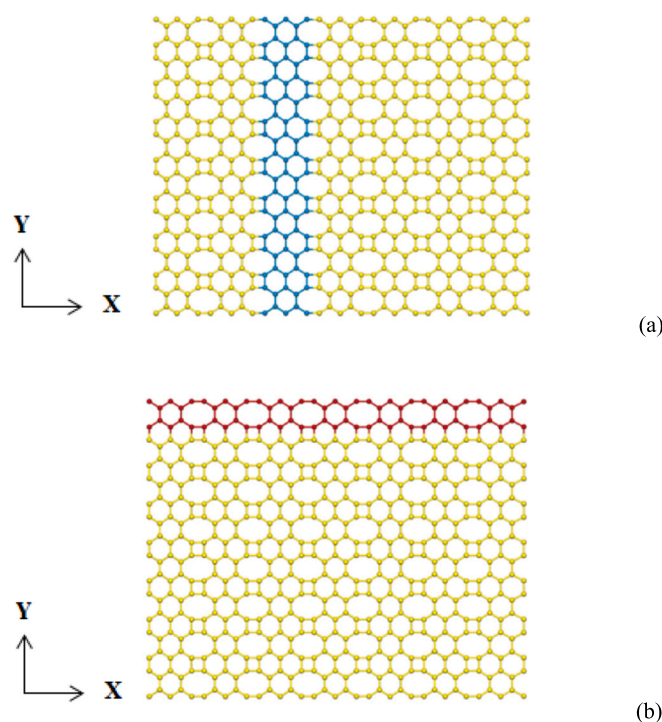


Fig. 2. The unit for nanoribbon investigation is called ('n'); (a) the unit ('n') is shown in blue varying in the X direction and (b) the unit ('n') is shown in red varying in the Y direction. (For interpretation of the references to colour in this figure legend, the reader is referred to the web version of this article.)

and sp -hybridized carbon atoms [23,24]. Graphyne and graphdiyne exhibit excellent attributes for potential applications such as nanofillers, transistors, semiconductor-metal hybrids, anisotropic conductors, and Li-ion batteries [25–27].

Furthermore, biphenylene is the name of a carbon allotrope that was experimentally synthesized in 1941 by Lothrop [28]. This structure, also known as Net C, has two close relatives, Net W and Net Y, all of which were theoretically predicted in 1997, 2013, and 2018, respectively [29,30]. The unit cells of Net C and Net Y are orthorhombic, while the unit cell of Net W is rhombic. Net C is the lightest allotrope among these types, and Net Y exhibits the highest atomic density. These carbon allotropes have zero band gap and metallic properties. Additionally, the

orientation of the rings differs in each structure, but all these allotropes contain 4-, 6-, and 8-membered carbon rings [31,32]. Yo and collaborators [33] indicate that the conductivity of Net W is perfectly preserved after Li adsorption. Its storage capacity can be about 4.5 times greater than that of the commercial graphite anode. Their detections suggest that Net W can be a remarkable anode candidate for use in lithium-ion batteries. Also, Hamzei et al. [34] reported the wettability characteristics of Net C, Net Y, and Net W, and theoretically presented values that can be named as the first approximation of the wettability properties of these allotropes.

Rong et al. [35] demonstrated anisotropic behavior in the mechanical properties and electronics of Net Y through molecular dynamics simulations. They reported the in-plane Poisson's ratio values, including $\nu_a = 0.199$ and $\nu_b = 0.212$ and the in-plane Young's modulus values, which are lower than the experimental counterparts for graphene, with $C_a = 318.88\text{N/m}$ and $C_b = 296.99\text{N/m}$ in the uniaxial directions a and b . Additionally, they presented the in-plane elastic constants along the a and b directions as $c_{11} = 332\text{N/m}$, $c_{22} = 311\text{N/m}$, $c_{12} = 66\text{N/m}$ and $c_{44} = 27\text{N/m}$. Their results indicated that Net Y represents more stable feature than the experimentally synthesized graphdiyne but metastable compared to graphene.

This study primarily focuses on predicting the mechanical characters of Net Y subjected to a tensile stress in uniaxial directions using the classical simulation of molecular dynamics (MD). Due to the high potential applications of carbon allotropes in various industries and their performance under sub-room and elevated temperature conditions, this study investigates Net Y over a temperature range from 10 K to 1000 K. In light of this, geometry effects and nanoribbon characterization have been examined to anticipate the further application of this nanosheet. Additionally, to bridge the gap between experimental and theoretical studies for more practical use, random defect densities ranging from 0.5 % to 3 % have been introduced to the nanostructure, considering vacancies without any stress concentration. These findings underline the cooperation between temperature gradients, defect density, and nanoribbon characterization in determining the mechanical behavior of nanomaterials. The study supplies valuable insights for optimizing Net Y design and performance in advanced materials applications.

The order of this study is introduced as follows: Section 2 presents the details of the carried out MD simulation as well as the model presentation. Section 3 discusses on tensile response subjected to the effects thermal gradients besides defect density and nanoribbon characterization. Accordingly, relevant to each case, the quantities of Young's modulus, failure strain and stress besides the strain energy are extracted. Further, the location of failure is also discussed. Finally, Section 4 gives the obtained concluding remarks.

2. Simulation technique and modelling approach

All tests are simulated using a large-scale atomic/molecular massively parallel simulator (LAMMPS) [36,37]. The structure's interconnections between atoms are expressed by the AIREBO potential, which describes all C–C atomic bonding. AIREBO [38] is an appropriate potential for covalent bonds between carbon atoms in nanostructures. It is noted that the AIREBO potential used in this study models bond stretching and thermal vibration accurately but does not capture oxidation or chemical interactions, making the results representative of inert conditions.

Material Studio software [39] designs the structure. Then, the coordinate file is converted to a readable data file for LAMMPS using MATLAB software. To establish the required thermodynamic equilibrium, the canonical ensemble (NVT) on the basis of Velocity-Verlet kind of the integrator algorithm, integrated with the Nose-Hoover thermostat methodology having a time step of 0.0005 ps is considered to certify a model of stable system and minimize the role of variation in the temperature [40–42]. To simulate the tensile testing, we minimized the energy of the whole system, and then the relaxation procedure was used

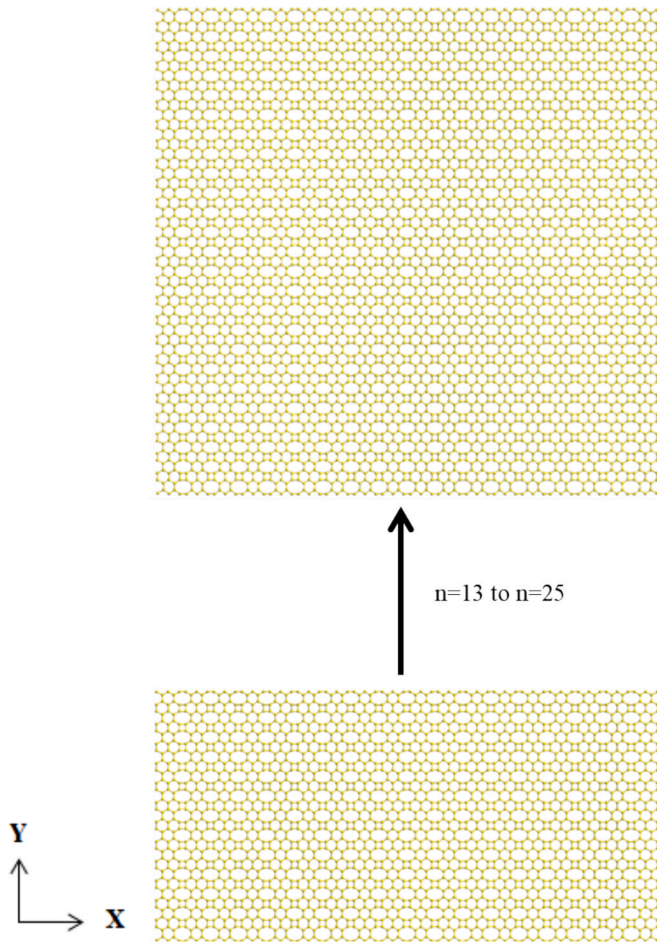


Fig. 3. Changing ('n') in the Y direction from ($n = 13$) to ($n = 25$), while the tensile displacement is applied in the X direction.

to achieve an equilibrium state, which took up to 0.5 ns. After this, we gradually applied 0.002 Å displacement in every stage of tensile testing simulation and we implemented a relaxation procedure to make the influence of stress concentration as few as possible. This process causes appropriate stress dispersion within the structure and it would be possible to control the effects of boundary caused by a failure. Stress, strain, and potential energy of the structures have been measured and tracked during the test.

In this article, an attempt has been made to study the variations in the mechanical characters of Net Y because of the effect of temperature gradient, vacancy defect, and effect size and geometry. A single layer nanosheet of Net Y, as depicted in Fig. 1 (front view), with a quantity of

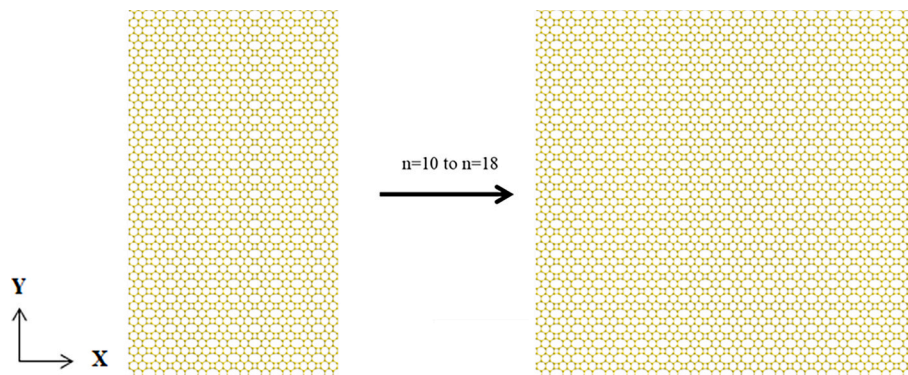


Fig. 4. Changing ('n') in the Y direction from ($n = 10$) to ($n = 18$), while the tensile displacement is applied in the X direction.

atoms including 4500 and targeted dimension of 109.378 Å in 112.122 Å for X and Y direction, is considered to simulate tensile test in different temperatures and defect investigation.

In order to investigate nanoribbons and predict the effect of geometry and size on the structure's mechanical characters, tensile tests were performed in X and Y directions in different ribbon dimensions. The nanoribbon dimensions are specified by ('n'), which shows a unit cell nanoribbon, Fig. 2. The quantity of ('n') along the X axis variation is 13, 16, 19, 22, and 25 while in the Y direction, is 10, 12, 14, 16 and 18. These configurations are depicted in Fig. 3 and Fig. 4, in the specified order. The size of nanoribbons in the X and Y directions is tabulated in Table 1 and Table 2, respectively.

MATLAB software was used to create vacancy defects in Net Y. Via using MATLAB coding, a specific number of atoms was removed from the structure, preventing decentralization. In this investigation, vacancy defects for each considered percentage were applied five times to the structure randomly, in such a way that each one could be tested independently, while the average of these simulations presented the related mechanical properties. These percentages were imposed on structures with 0.5 %, 1.0 %, 1.5 %, 2.0 %, 2.5 %, and 3.0 % vacancy defect density. Fig. 5 represents the Net Y nanostructure having a 3.0 % vacancy defect density.

Eventually, mechanical properties such as failure stress as well as strain, Young's modulus, and strain energy are showcased and analyzed. Moreover, the relevant stress-strain path is traced and presented up to the failure point for each investigation. Using the stress-strain diagram, the Young's modulus is extracted by calculating the slope of the stress-strain curve up to 3 % strain. Finally, the allocated strain energy is

Table 1

The size of nanoribbons varies along with the Y direction and the tensile load is applied in the X direction.

n	width (Å)	Length (Å)
13	55.986	112.122
16	69.170	112.122
19	82.354	112.122
22	95.528	112.122
25	109.378	112.122

Table 2

The size of nanoribbons varies in the X direction and the tensile test is applied along with the Y direction.

n	width (Å)	Length (Å)
10	109.378	61.626
12	109.378	75.760
14	109.378	86.730
16	109.378	99.284
18	109.378	112.122

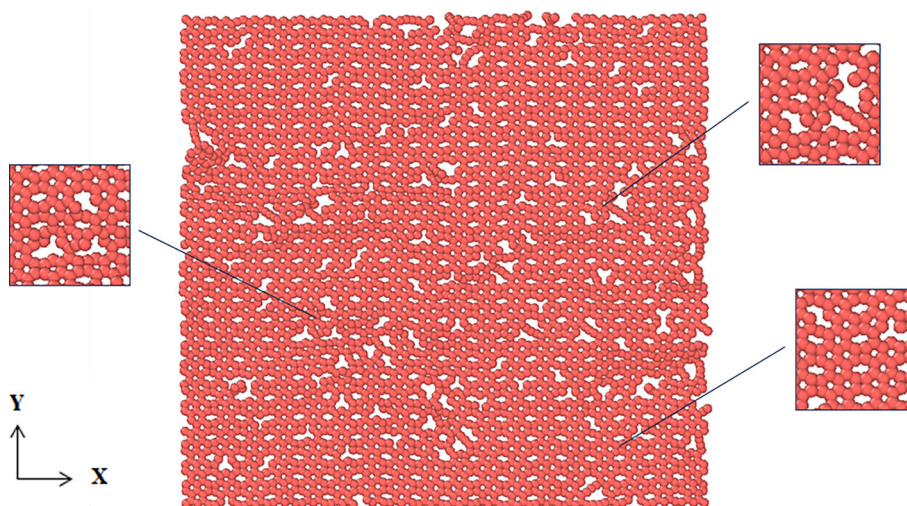


Fig. 5. The application of 3% of vacancy defects in the structure.

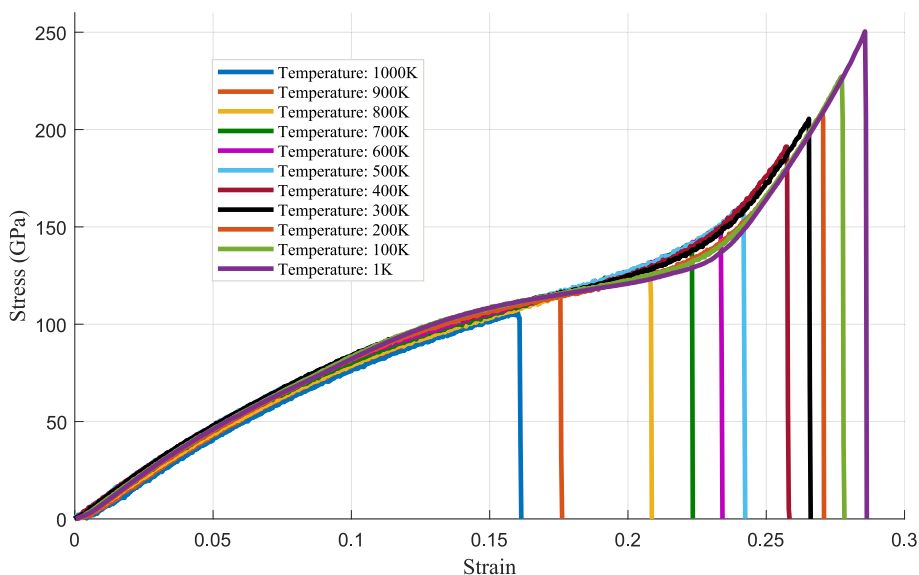


Fig. 6. Stress–strain curve in the X direction for temperatures including 1 K to 1000 K.

calculated using the trapezoidal rule to estimate the area under the stress–strain curve.

3. Numerical outcomes and discussions

This part of the exploration includes three chief subsections. First, the mechanical properties of the Net Y nanosheet, namely as Young's modulus, maximum tensile stress as well as maximum strain, and the strain energy under uniaxial tension, are examined across a temperature range of 1 K to 1000 K in 100 K increments. These properties, calculated from stress–strain relationships, are analyzed along the X and Y axes to capture the nanosheet's anisotropic behavior. Afterwards, the tension dispersion in a single-layer Net Y structure is investigated at 300 K for both directions, providing insights into the nanosheet's integrity and failure mechanisms. Then, the results are validated by comparing them with prior studies, demonstrating good agreement and highlighting the reliability of this study.

Second, an extensive exploration on the defective Net Y sheets is carried out with the aid of the classical MD simulations. In this regard, the stress–strain path of a perfect Net Y structure is illustrated. Moreover, the role of defect density in the values of abovementioned

mechanical characters is explored comprehensively. In addition, for the defect density characterization analysis, the directions of tensile loading condition applied to the nanosheet are along with the both X and Y axes. Third, the nanoribbon study and geometry effect are presented, taking all abovementioned extracted mechanical characters into consideration.

The aim of introduction of vacancy defects randomly is to emulate the stochastic nature of defect formation in real experimental conditions, such as high-energy irradiation, thermal fluctuations, or non-equilibrium fabrication processes. The randomness reflects the unpredictable spatial distribution of atomic vacancies that often arise in practical scenarios where synthesis control is limited. This method allows for the investigation of mechanical response trends under disordered conditions, rather than assuming idealized or artificially constrained defect configurations. This approach is widely adopted in molecular dynamics studies to provide statistically averaged insights into the effect of defect density on mechanical properties [43].

3.1. Gradient temperature effect

This section investigates the effects of temperature on maximum stress and strain as well as the toughness and Young's modulus of Net Y

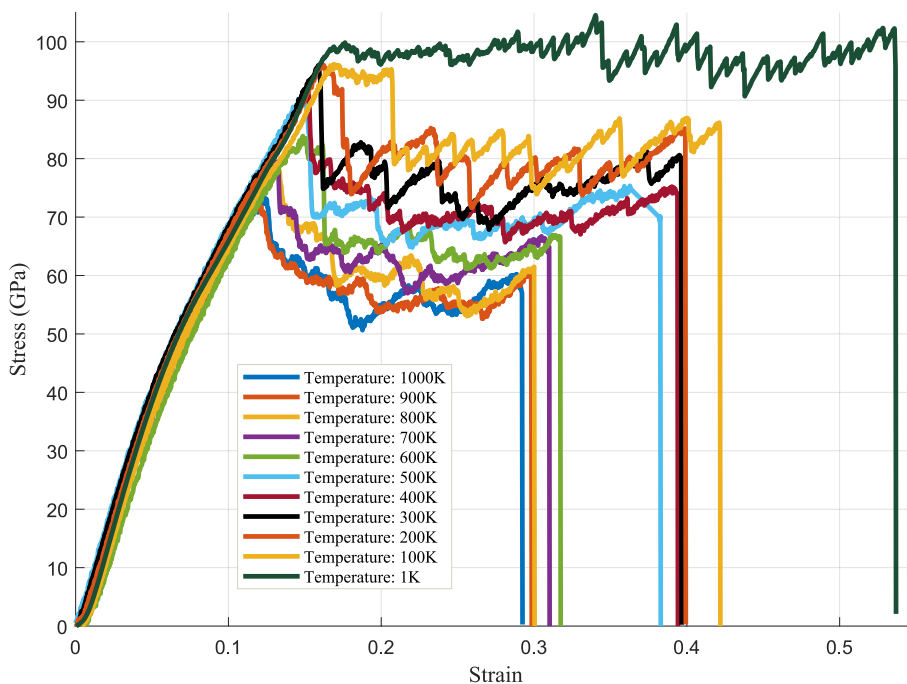


Fig. 7. Stress–strain curve in the Y direction for temperatures including 1 K to 1000 K.

Table 3

Failure stress, failure strain, along X direction; first failure stress, first failure strain, ultimate failure stress, ultimate failure strain along Y direction for temperatures including 1 K to 1000 K.

Temp (K)	Fail Stress X (GPa)	Fail Strain X	First Fail Stress Y (GPa)	First Fail Strain Y	Ult Stress Y (GPa)	Ult Strain Y
1	250.394	0.286	104.540	0.340	101.800	0.535
100	227.269	0.277	96.176	0.169	85.930	0.421
200	209.245	0.270	96.002	0.162	84.290	0.398
300	205.530	0.265	95.989	0.159	80.600	0.395
400	191.267	0.257	91.216	0.151	74.590	0.392
500	161.070	0.242	90.940	0.149	69.980	0.381
600	150.655	0.233	83.860	0.149	66.680	0.341
700	141.052	0.223	79.480	0.132	65.940	0.309
800	130.668	0.207	78.160	0.130	61.030	0.299
900	116.164	0.174	72.391	0.117	59.980	0.297
1000	106.440	0.160	71.019	0.116	58.250	0.291

nanosheet. Accordingly, the nanosheet is considered under various temperature changes from 1 K to 1000 K, in conjunction with applying a uniaxial tensile stress. Fig. 6 presents stress–strain curves for tensile loading along the X axis, and Fig. 7 illustrates the corresponding curves along the Y axis. The results indicate that the stress and strain at failure decrease in the X direction as temperature increases. Although the failure trend along the Y axis also shows a decrease with temperature, the stress–strain curves exhibit a pronounced failure region after the first failure. This study distinguishes between the first failure and the ultimate failure in terms of stress and strain for tensile loading in the Y direction. Additionally, the results reveal the anisotropic behavior of the nanosheet. Along the X axis, the ultimate failure coincides with the first failure, whereas in the Y direction, these failures occur at distinct points.

Table 3 presents the quantities of the failure stress and strain along the X axis, and first failure stress as well as failure strain besides the ultimate failure stress as well as ultimate failure strain attributed to the Y axis. Relevant to the X axis, the stress and strain get their peak quantities in order at 1 K, with 250.39GPa and 0.2857. This variation becomes lower via the temperature growth. From 1 K to 300 K, stress and strain

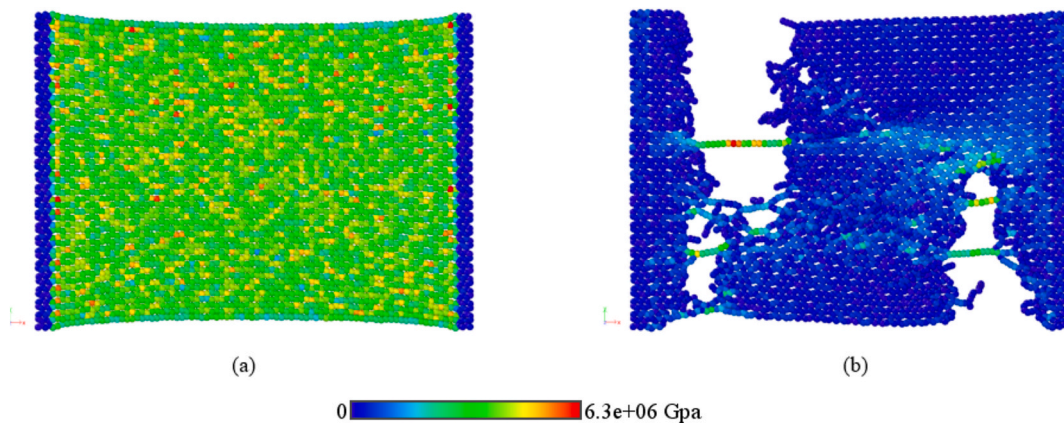


Fig. 8. Stress distribution for 300 K under tensile load along X direction: a) stress distribution in the nanosheet before the failure; b) stress distribution in the nanosheet after the failure.

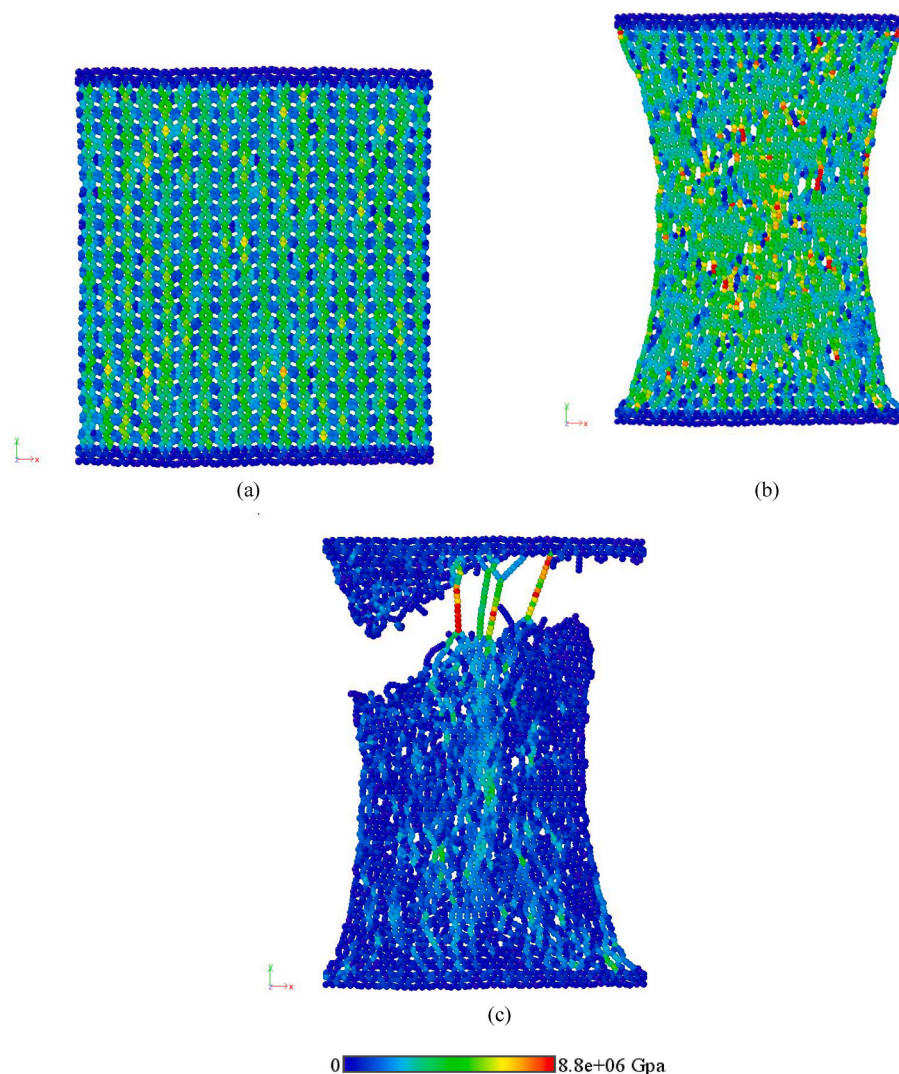


Fig. 9. Stress distribution for 300 K under tensile load along Y direction: a) stress distribution in the nanosheet before the first failure; b) stress distribution in the nanosheet after the first failure and before the ultimate failure; c) stress distribution in the nanosheet after the ultimate failure.

decrease by about 44GPa and 0.02, and beyond this point, from 400 K to 1000 K, it shows about 84GPa and 0.09 decrease, for stress and strain, separately. For the Y direction, both trends of first failure and ultimate failure decline due to temperature growth. They reach their largest value at 1 K, including 104.54GPa, 0.34, 101.80GPa, and 0.53, for first failure stress, first failure strain, ultimate strain, and ultimate failure, respectively. Although the trend of both first failure and ultimate failure values falls down by temperature growth, the trend process doesn't show the same manner. For instance, for the first failure stress, the values show a slight drop in the ultimate stress from 100 K to 500 K indicating about a one-third change compared to the ultimate value. Therefore, material behavior changes in the failure zone before occurring it in Y direction tension displacement.

The temperature-dependent decline in failure stress and strain observed in Figs. 6 and 7 can be attributed to increased atomic vibrations at elevated temperatures, which reduce bond stability and promote earlier bond rupture. This behavior is typical of molecular dynamics (MD) simulations and reflects the intrinsic thermal response of the material under ideal, inert conditions. The use of the AIREBO potential captures bond dissociation and local thermal effects but does not model environmental factors such as oxidation or long-term structural degradation. Consequently, these results provide insight into the inherent mechanical resilience of Net Y rather than a direct quantitative match to

experimental systems.

The results indicate that the nanostructure exhibits significant stability with brittle behavior along the X axis, characterized by abrupt failure under stress. In contrast, the Y direction demonstrates greater strength and ductility, as evident from the extended failure region in the stress-strain curves. Fig. 8 illustrates the tension distribution before and after failure along the X direction at 300 K, where the failure stress and strain are 205.53GPa and 0.26, respectively. Fig. 8(a) shows the tension distribution before failure, demonstrating how the nanosheet endures the applied tension integrity all over it. This distribution highlights the material's remarkable resistance to loading along the X direction. Fig. 8 (b) indicates the tension distribution of this nanosheet after the failure which shows that the nanosheet failed in two locations simultaneously. Fig. 9 depicts the tension distribution along the Y direction, with the values for first failure stress, first failure strain, ultimate failure stress, and ultimate failure strain being 95.98GPa, 0.158, 80.60GPa, and 0.39, respectively. Fig. 9(a) shows the tension distribution in the nanosheet just before the first failure, where the carbon chains with six-membered rings bear the majority of the imposed tension, while the chains with eight-membered rings endure less. After the first failure, which manifests as defects and porosity in the nanosheet, the tension is redistributed, as illustrated in Fig. 9(b), with combined tension experienced around the emerging vacancies. Finally, after the ultimate failure, the

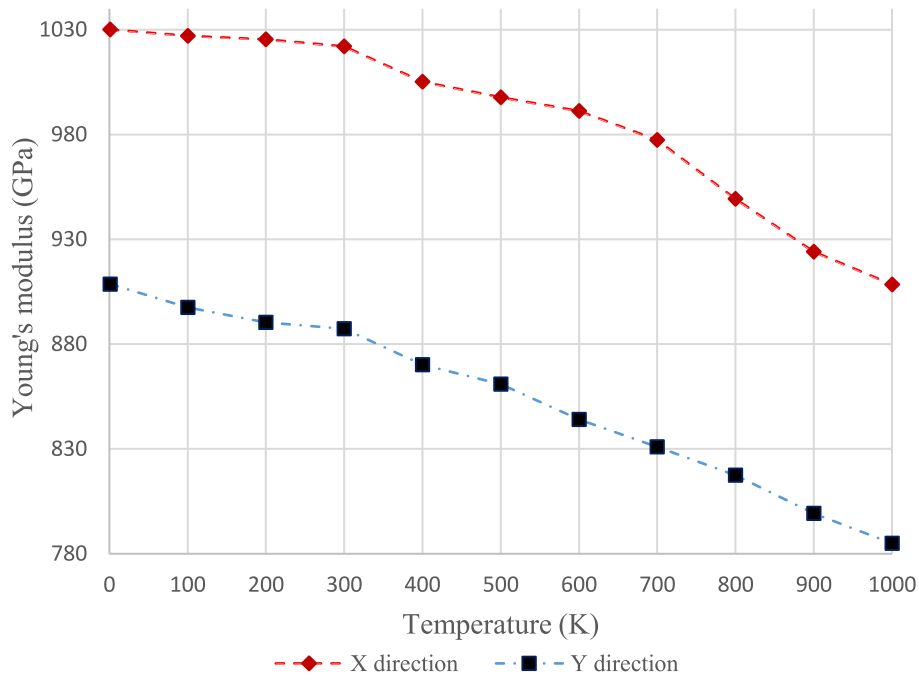


Fig. 10. Young's modulus values per temperature variation from 1 K to 1000 K, for tensile displacement imposed in the X and Y direction.

Table 4

Elastic's properties in the X direction and Y direction for this study and Ref. [35] and corresponding error.

Directions	This study's Young's modulus (GPa)	Ref. [35] In-plane Young's modulus (N/m)	Error (%)
X	1022.00	318.88*	12 %
Y	887.31	296.99*	18 %

* In order to change the in-plane Young's modulus given by Ref. [35] to the standard Young's modulus, it is divided to the thickness value of the modeled Net Y nanosheet.

nanosheet undergoes complete structural destruction, as shown in Fig. 9 (c). Overall, this nanosheet demonstrates significantly higher failure stress and strain along the X direction compared to the first failure values in the Y direction. Specifically, at 300 K, the failure stress along with the X direction is more than twice that of the Y direction's first failure stress. At higher temperatures, such as 800 K and 900 K, this ratio reduces slightly, reaching approximately 1.5 times the first failure value. Additionally, the failure strain along the X direction consistently remains around 1.5 times greater than the first failure strain along with the Y direction across the investigated temperature range. Furthermore, the ultimate stress and strain values in the Y direction are lower than the first failure stress and strain.

Fig. 10 illustrates the quantities of Young's modulus in the presence of the temperature gradient along with the X and Y axes. Associated with

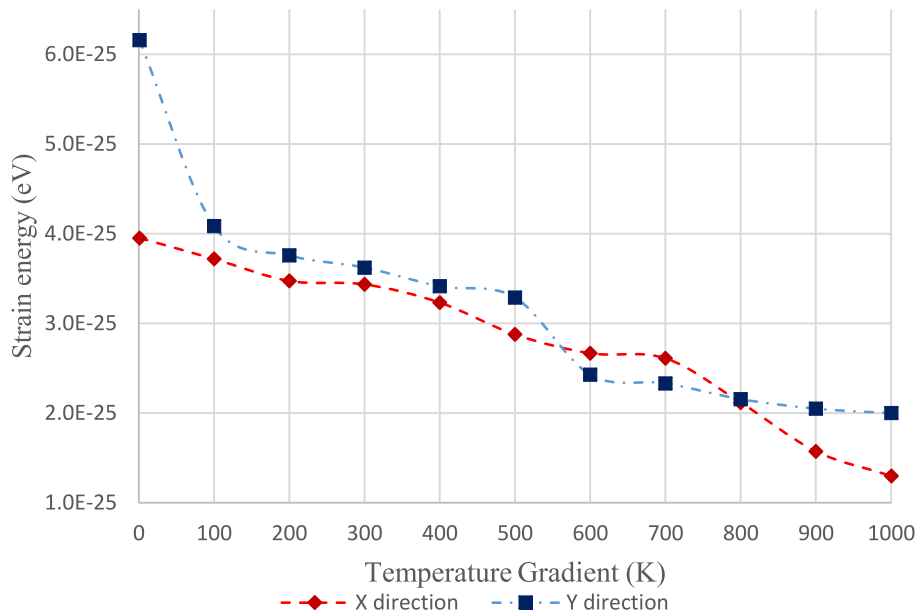


Fig. 11. Strain energy values per temperature variation from 1 K to 1000 K, for tensile displacement imposed in the X and Y direction.

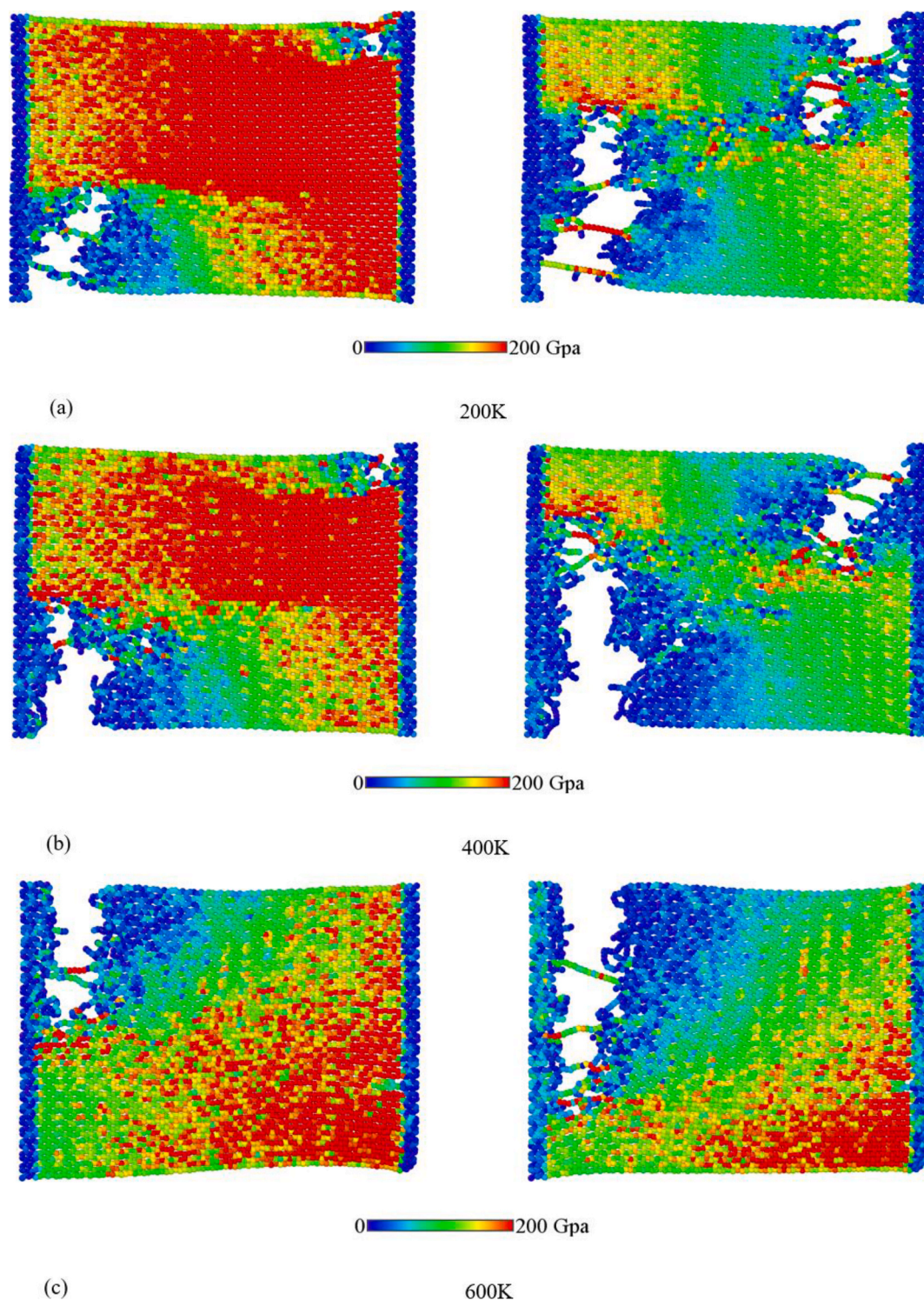


Fig. 12. Distinct temperature variation, stress distribution and failure initiation in Net Y along with X direction: (a) 200 K, showing initial bond rupture at the upper-right edge and subsequent crack propagation toward the lower-left; (b) 400 K, with failure nucleating at the lower-left edge and advancing toward the upper-right; (c) 600 K, where the first crack appears at the upper-left edge and propagates diagonally toward that direction.

the X axis (red line), a temperature rise causes a decline in the elastic modulus. The highest value is observed at 1 K with 1030.10GPa, while the lowest value is recorded at 1000 K with 908.47GPa. Notably, the decrease is more pronounced from 500 K to 1000 K, showing a drop of approximately 89GPa, compared to a smaller decline of 32GPa from 1 K to 400 K. This trend indicates that higher temperatures have a greater impact on the stiffness and Young's modulus along the X direction. For the Y direction (blue line), the highest Young's modulus value is

908.66GPa at 1 K, while the lowest is 784.95GPa at 1000 K. The decline is almost linear between 500 K and 1000 K, with a reduction of 76GPa, which is nearly twice the drop observed between 1 K and 400 K (about 38GPa).

In Fig. 10, the retention of approximately 80–85 % of the Young's modulus up to 1000 K suggests that Net Y possesses strong thermoelastic properties. This thermal stability arises from its hybrid sp²–sp bonding configuration, where rigid sp-hybridized carbon chains resist bond

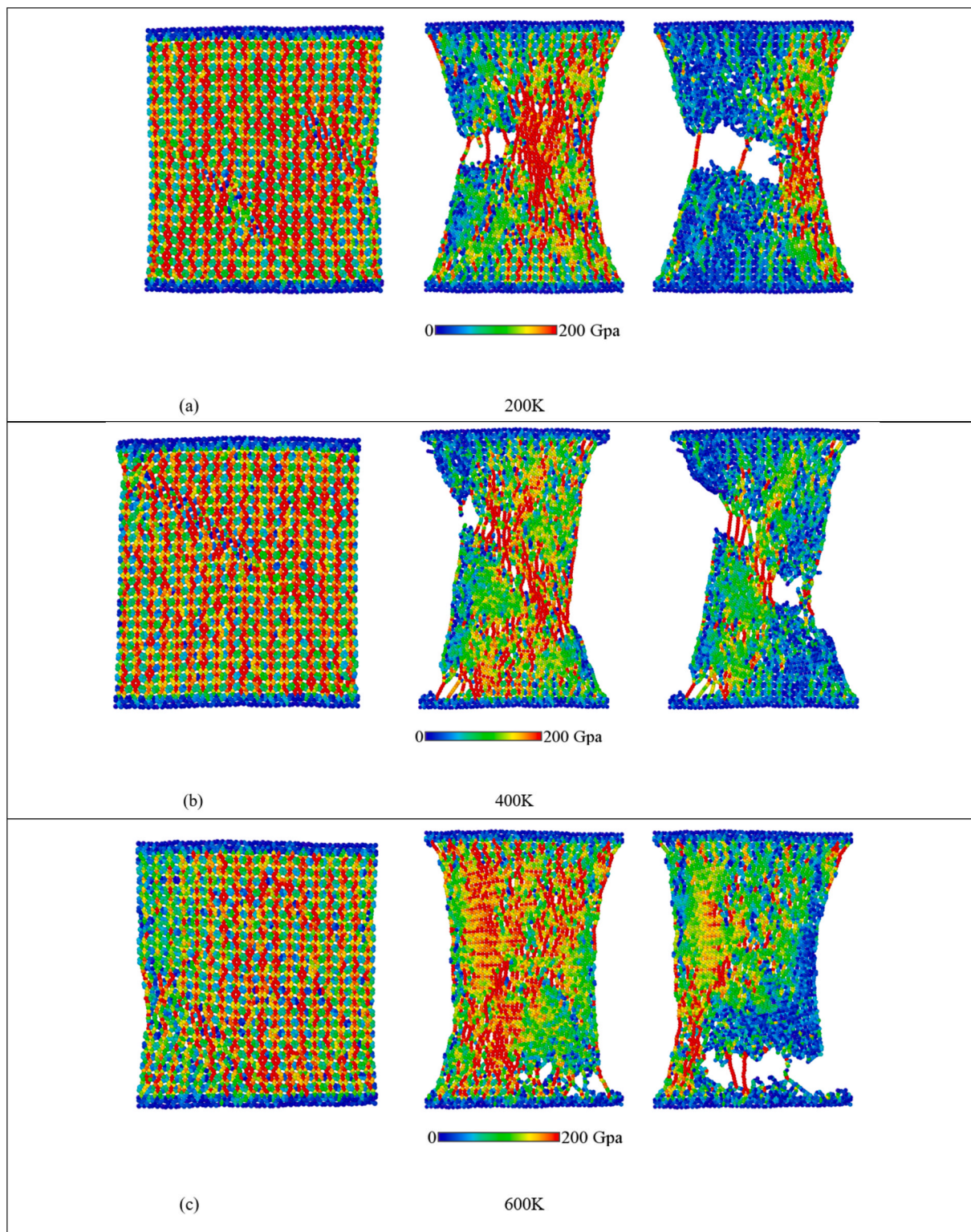


Fig. 13. Distinct temperature variation, stress distribution and failure initiation in Net Y along with Y direction: (a) 200 K, showing initial bond rupture at the left-middle edge and propagation toward the sheet’s center; (b) 400 K, with failure nucleating again at the left-middle edge, right-bottom and advancing into the central region; (c) 600 K, where the first crack appears at the bottom-right corner and propagates inward.

rotation and sp² rings help redistribute stress. This behavior is consistent with previous simulations on similar carbon allotropes, such as graphyne, which also exhibit modest stiffness reduction at high temperatures. Compared to graphene, where phonon scattering leads to more substantial softening, Net Y’s multi-ring structure may damp such effects, offering improved mechanical integrity at elevated temperatures

[44–46].

In a general view, the quantities of Young’s modulus along with the X axis are consistently higher than those along with the Y axis. For an instance, at 300 K, the quantities of Young’s modulus in order are 1022GPa and 887.31GPa along with the X and Y axes. Also, in the Rong et al. study [35], the in-plane Young’s modulus were extracted as $C_a =$

Table 5

Vacancy statistics for Net Y nanosheets (The table lists the total number of carbon atoms removed at random to achieve each target vacancy concentration, expressed as a percentage allocated to the 4500 atoms of the pristine nanosheet).

Vacancy defect (%)	Number of removed atoms (Vacancies)
0.5	22
1	45
1.5	67
2	90
2.5	112
3	135

318.88N/m and $C_b = 296.99N/m$. Comparing these values with the current findings reveals good agreement, with error rates of approximately 12 % and 18 % along with the X and Y axes, respectively, as summarized in Table 4.

Strain energy variation per temperature gradient is illustrated in Fig. 11. The value of strain energy decreases as the temperature rises, in both directions. As shown in red, this decline occurs more moderately. In the Y direction, as represented in blue, has a more significant influence on the nanosheet than in the X direction. The results show $3.43 \times 10^{-25}eV$ and $3.62 \times 10^{-25}eV$ for the tensile loading along the X and Y directions, respectively. This variation highlights the greater sensitivity of the nanosheet's structural integrity to temperature changes,

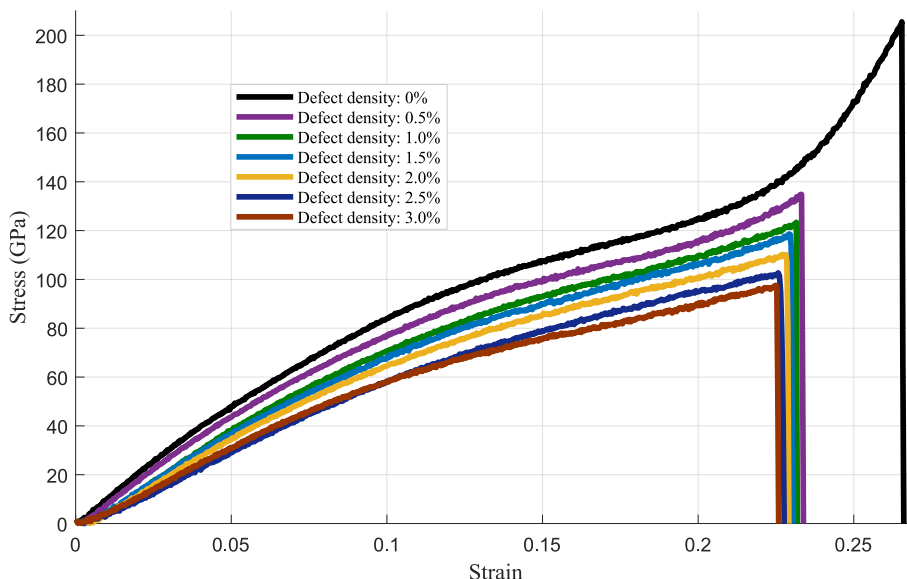


Fig. 14. Stress–strain curve in the X direction for the defect densities including 0 % to 3 % (these curves represent averaged results from multiple random defect configurations at a fixed temperature, offering an approximate view of how failure stress and strain evolve with increasing defect density).

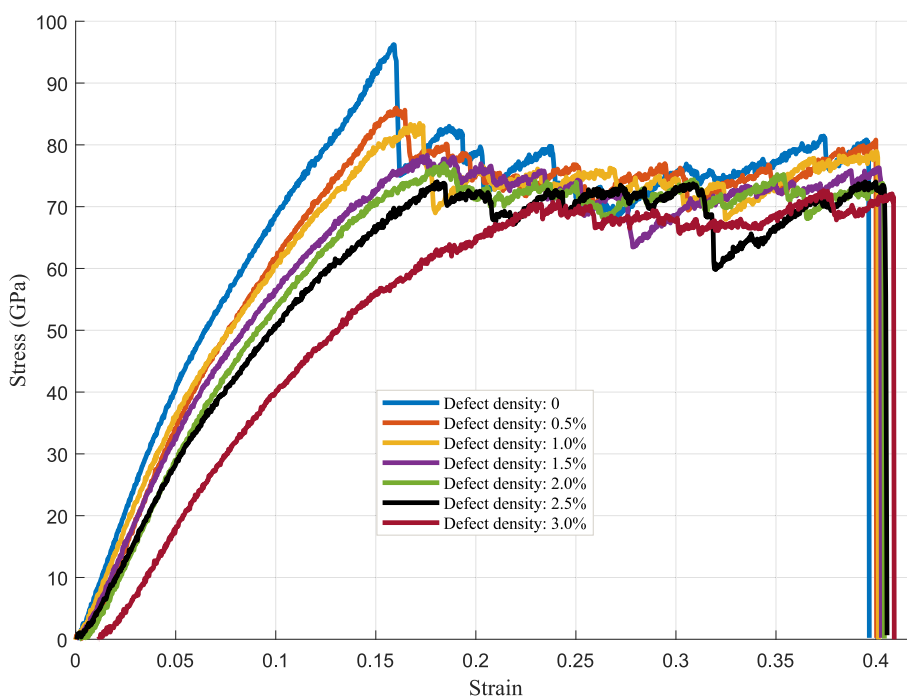


Fig. 15. Stress–strain curve in the Y direction for the defect densities including 0% to 3% (these curves represent averaged results from multiple random defect configurations at a fixed temperature, offering an approximate view of how first and ultimate failure stress and strain evolve with increasing defect density).

Table 6

Failure stress, failure strain, along X direction, plus first failure stress, first failure strain, ultimate failure stress, ultimate failure strain along Y direction for defect density percentage including 0 % to 3 %.

Defect Density %	Fail Stress X (GPa)	Fail Strain X	First Fail Stress Y (GPa)	First Fail Strain Y	Ult Stress Y (GPa)	Ult Strain Y
0 %	205.53	0.265	95.988	0.159	80.600	0.395
0.5 %	134.80	0.233	85.982	0.160	80.530	0.399
1 %	123.398	0.231	83.490	0.171	78.770	0.400
1.5 %	118.609	0.229	78.766	0.176	76.320	0.401
2 %	110.274	0.227	76.980	0.180	76.060	0.402
2.5 %	102.688	0.226	76.270	0.181	73.460	0.403
3 %	97.587	0.225	63.320	0.188	71.570	0.408

particularly along the Y direction, where the ability to store strain energy drops more intensely.

3.2. Failure locations and stress distributions per distinct temperatures

Fig. 12 illustrate the tension distribution and failure initiation sites in the X direction at 200 K, 400 K, and 600 K, respectively. At 200 K (Fig. 12.a), stress localizes at the upper-right edge, where the first bond ruptures; this crack then propagates toward the lower-left, culminating in complete fracture. At 400 K (Fig. 12.b), the fracture sequence reverses: initial failure nucleates at the lower-left edge and subsequently advances toward the upper-right, indicating that moderate thermal activation shifts the region of maximal stress. At 600 K (Fig. 12.c), bond breakage begins at the upper-left edge, demonstrating that increased atomic vibrations at higher temperatures preferentially weaken edge bonds.

Fig. 13 present the analogous results for the Y direction. At 200 K (Fig. 13.a), fracture initiates at the left-middle edge, with the crack front propagating into the sheet's center. At 400 K (Fig. 13.b), failure again starts at the left-middle, but the crack advances more directly into the central region and then in the left-bottom, reflecting that thermal softening accelerates crack growth after nucleation. At 600 K (Fig. 13.c), failure originates at the bottom-right corner and propagates upward across the sheet, indicating that corner bonds become the weakest links under high thermal activation.

Thermal activation, as shown by Zhao et al. [47], reduces the energy barrier for bond rupture at edge sites where stress is concentrated, and Zhang et al. [48] found that raising the temperature can lower graphene's fracture stress by approximately 66 %. In the Net Y nanosheet, the edges likewise serve as thermal weak points: failure initiates at different sites (for example, the upper-right at 200 K and the lower-left at 400 K) and then propagates anisotropically, mirroring these core findings. In addition, the animation of failure of Net Y, for temperatures including 200 K, 400 K, and 600 K in both X and Y direction are presented in the [supplementary S1 to S6](#).

3.3. Defect density effect

In this part of study, a detailed analysis is presented on the influence of defect density percentages on the quantities of the Young's modulus, ultimate stress as well as strain, and strain energy of Net Y nanosheets. The defect densities randomly examined include 0.5 %, 1 %, 1.5 %, 2 %, 2.5 %, and 3 % of the number of atoms of the nanosheet. Table 5 provides a clear quantitative summary of how many atoms are randomly deleted to attain each specified vacancy density in the presented simulations. The examination is covered independent explorations attributed to the uniaxial tensile loading along with X and Y axes, with comparisons made to the pristine nanosheet structure. For reliability, all investigations were repeated at least five times. The findings are presented and analyzed as follows.

Stress–strain curves for defect densities of 0 %, 0.5 %, 1 %, 1.5 %, 2 %, 2.5 %, and 3 % in the X direction are presented in Fig. 14. In comparison with the pristine structure, the failure happens earlier across all paths, demonstrating a consistent decrease in ultimate stress and strain values with increasing defect density. Similarly, Fig. 15 illustrates stress–strain curves at the same defect densities for the Y direction. As defect density increases, the values of first failure stress and ultimate failure stress show a decline, while the values for strain, ultimate and first failure, grow.

For investigating defects along the X direction, the results show that as the defect percentage increases, the stress reaches just over half of the value observed in the pristine nanosheet. Similarly, the strain decreases, but more gradually than the stress, with a reduction of approximately 15 %. The results show that the nanosheet endures from tensile loading decrease as the random defect vacancy increases along with the X axis. On the contrary, for the Y direction, the first failure and ultimate failure stresses also illustrate the dropping trend in the values, but strain faces a slight increase. The first failure and ultimate failure stresses indicate 32.66GPa and 9.03GPa, respectively, decrease when the defect density is 3 %. The first failure strain and ultimate failure strain, present an incline trend, about 15 % and 3 %, with the most imposed random defect density in this study. The data related to the failure stress and strain along the X direction, the first failure stress as well as strain, and ultimate failure stress as well as strain along the Y direction is presented in Table 6.

Growing strain values including first and ultimate failure, highly depended on the location of defects and densities applied to the nanosheet. Although depending on the location of the defect can vary intensely in some case the standard deviation of each five MD simulations, mechanical properties, but in overall the results shows as the defect growth, first failure and ultimate failure stress reduce and related strains get higher, which it means the strength ability of the nanosheet get higher. Fig. 16 shows a 2.5 % defect vacancy applied to the Net Y. Fig. 16(a), shows the vacancies in the structure before the first failure, Fig. 16(b), indicates the holes, getting larger as the nanosheet get into the failure zone, and Fig. 16(c), demonstrates that the failure happens from where the hole imposed. In the pristine nanosheet, just before the first failure, where the carbon chains with six-membered rings bear the majority of the imposed tension, while the chains with eight-membered rings endure less. After the first failure, which manifests as defects and porosity in the nanosheet, the tension is redistributed with combined tension experienced around the emerging vacancies and after the ultimate failure, the nanosheet undergoes complete structural destruction. But by imposing vacancy to the nanosheet, this pattern in distribution tension before the first failure is disordered as shown in Fig. 16(d). By entering the nanosheet in the failure region and getting larger these defect holes, the tension is highlighted in the boundaries of the holes then other locations which is shown in Fig. 16(e) and finally failure happens in that location which is shown in Fig. 16(f). This phenomenon highly depended on the location of the defect and the amount of defect on the nanosheet and can vary values significantly as these parameters change. Fig. 17(a) to Fig. 17(d), shows another 2.5 % random defect imposed Net Y, with different locations of holes. As presented the process of tension distribution vary as the location of failure changes.

Fig. 18 illustrates the variation of Young's modulus with defect density percentages under tensile loading along with the X axis. It is found that through an increment in the defect density, the Young's modulus exhibits a noticeable decline. For instance, allocated to the defect density equal to 0.5 %, the quantity of the Young's modulus is 963.65GPa. While allocated to the defect density equal to 2 %, it decreases to 791GPa. These values represent averages obtained from multiple simulations corresponding to per percentage of the defect density. Similarly, the trend of decreasing Young's modulus is observed along with the Y axis subjected to a tensile loading condition. Allocated to the defect density equal to 1.5 %, the quantity of Young's modulus is 715.1GPa, and it further reduces to 638.5GPa relevant to the defect

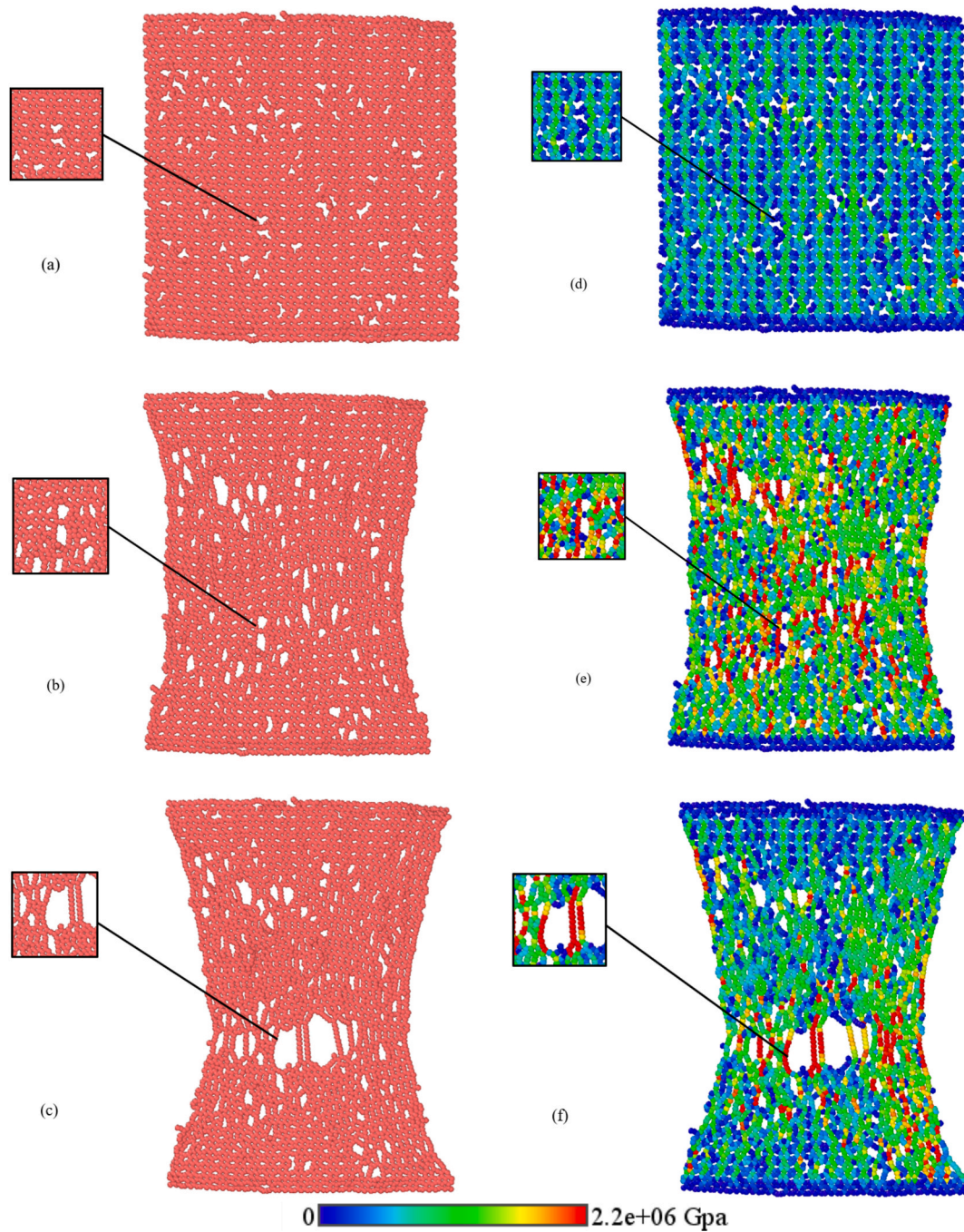


Fig. 16. The process of failure in the first 2.5% random defect imposed Net Y, during tensile displacement applied along Y direction. (a,d) defect densities besides its stress distribution imposed to the nanosheet; (b,e) defect densities besides its stress distribution getting larger in the failure zone; (c,f) picturing the failure happening besides its stress distribution from where the vacancy happened.

density equal to 2 %. In a general view, the quantities of Young's modulus along with the X axis are consistently more than those along with the Y axis. For example, at a 1 % defect density, the difference between the two directions is 78.02GPa.

Fig. 19 illustrates the variation of strain energy with defect density percentages under tensile loading condition along with the X axis. It is observed that through increasing the defect density, the quantity of the strain energy decreases. For example, at 0.5 % defect density, strain energy is $3.43 \times 10^{-25} eV$ while at 2 % defect density, it reduces to $2.1 \times 10^{-25} eV$. These values represent averages obtained from multiple simulation runs for each defect density percentage. A similar trend is observed in the Y direction, where strain energy decreases with

increasing defect density. Allocated to the defect density equal to 1.5 %, the quantity of strain energy is $3.35 \times 10^{-25} eV$, and allocated to 3 %, it declines to $2.97 \times 10^{-25} eV$. In a general view, the strain energy values along with the Y axis are consistently more than those along with the X axis. To mention an instance, allocated to the defect density equal to 1 %, the strain energy values associated with the two axes differ about $1.24 \times 10^{-25} eV$.

3.4. Classification of vacancies based on the atomic site

To further characterize the impact of vacancy location, the considered defects are classified according to the inequivalent atomic sites

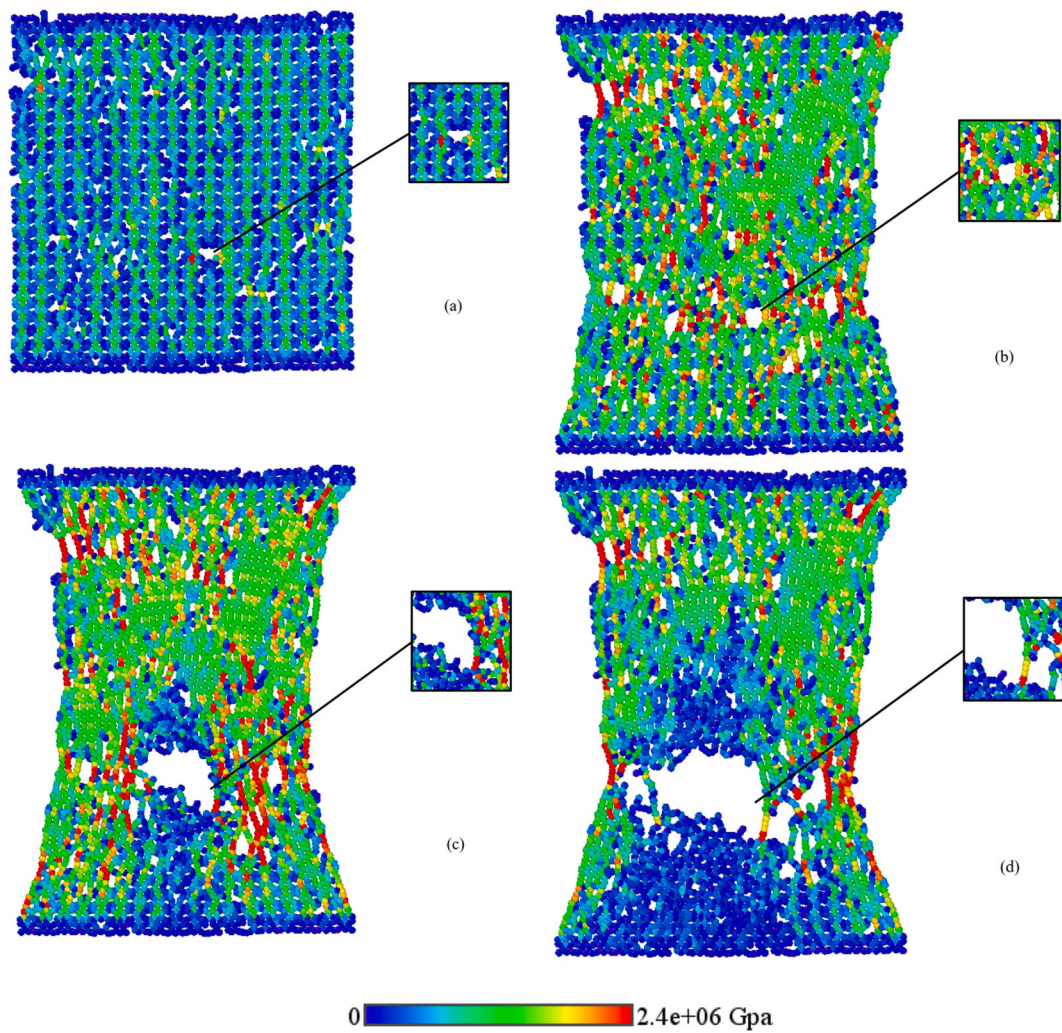


Fig. 17. The process of failure in the second 2.5% random defect imposed Net Y, during tensile displacement applied along Y direction, (a) defect densities imposed to the nanosheet, (b) defect densities getting larger in the failure zone, (c) and (d) the failure happens from where the vacancy happened.

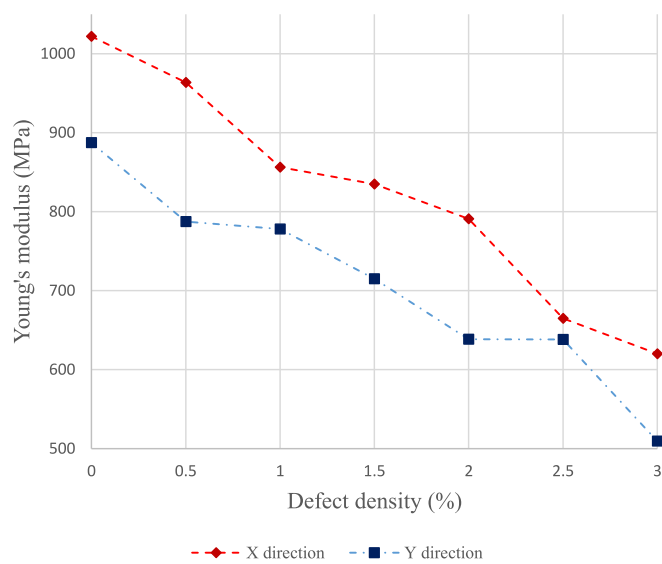


Fig.18. Young's modulus per defect density percentage including 0%, 0.5%, 1%, 1.5%, 2%, 2.5%, and 3% in the uniaxial directions.

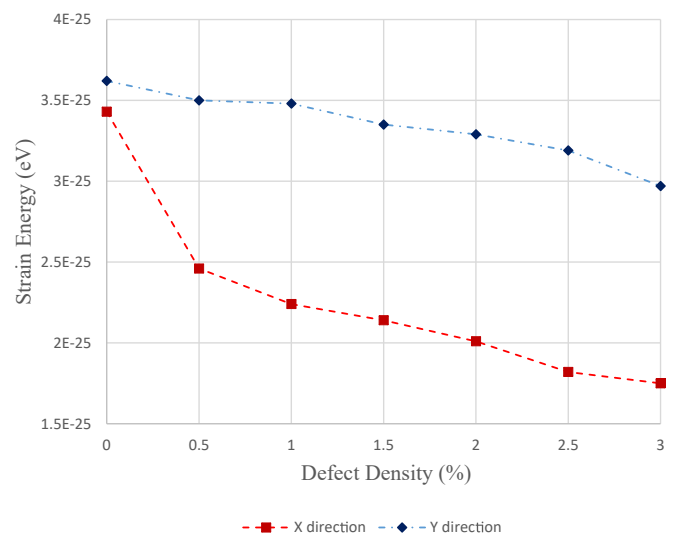


Fig.19. Strain energy per defect density percentage including 0%, 0.5%, 1%, 1.5%, 2%, 2.5%, and 3% in the uniaxial directions.

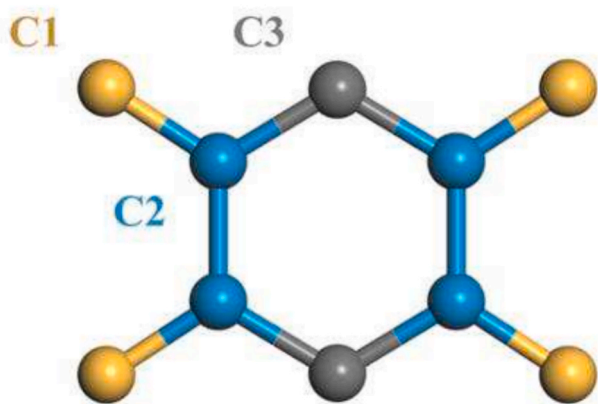


Fig. 20. Depiction of the three inequivalent carbon atom sites (C1, C2, and C3) in the Net Y lattice.

within the Net Y lattice. Following Rong et al. [35], carbon atoms can be categorized into three distinct sets: C1, C2, and C3 as shown by Fig. 20. Separate simulations are performed where a 1.5 % vacancy concentration is applied exclusively to each atomic type as illustrated in Fig. 21 (a–c). This approach isolates the mechanical influence of vacancies based on their specific lattice position as well as the local coordination.

Figs. 22 and 23 together with Tables 7 and 8 demonstrate the attributed stress–strain responses as well as the derived mechanical properties which reveal the site-dependent variations in the failure behavior and modulus degradation compared to the both pristine structures and the original random vacancy model. The stress–strain response is depicted along with the X–direction for the pristine Net Y (in blue) versus the Net Y with 1.5 % vacancy defects at each of the three inequivalent carbon sites: C1 (in orange), C2 (in gold), and C3 (in

purple). The pristine lattice achieves the highest stiffness and ultimate tensile strength. Moreover, introducing the vacancies at C1, C2, C3 results in to reduce the mechanical properties. This systematic trend highlights how vacancy location within the Net Y lattice governs its mechanical performance. Also, Fig. 23 quantifies the mechanical degradation induced by progressively severe defect configurations (C1, C2, and C3) in graphene under uniaxial tension along with Y direction.

Table 7 presents the mechanical properties of the pristine Net Y structure compared to the defected structures with 1.5 % vacancy defects at the C1, C2, and C3 atomic sites along with X direction. The pristine structure shows the highest failure stress, failure strain, Young’s modulus, and strain energy. In contrast, introducing defects at specific sites leads to notable reductions in all mechanical properties. Among the defected cases, vacancies at the C3 sites result in the lowest failure stress and Young’s modulus, indicating a greater weakening effect compared to C1 and C2.

Table 8 summarizes the mechanical properties of pristine Net Y and the defected structures with 1.5 % vacancies at C1, C2, and C3 sites, including first and ultimate failure stresses and strains, Young’s modulus, and strain energy along with Y direction. The pristine structure shows the highest stiffness, while defects especially at C2 and C3 significantly reduce stiffness and initial stress. However, C2 and C3 defects exhibit slightly increased first and ultimate strain rather than pristine Net Y.

The spatially random distribution of vacancies in our model reflects the intrinsic disorder observed experimentally in synthetic 2D carbon materials. Vacancy defects form inherently during synthesis and processing and remain present even in the most carefully optimized samples. Experimental and theoretical studies show that these vacancies distribute randomly and evolve dynamically under real-world conditions. Consequently, adopting a fully randomized vacancy-insertion scheme allows our simulations to accurately mirror the intrinsic disorder

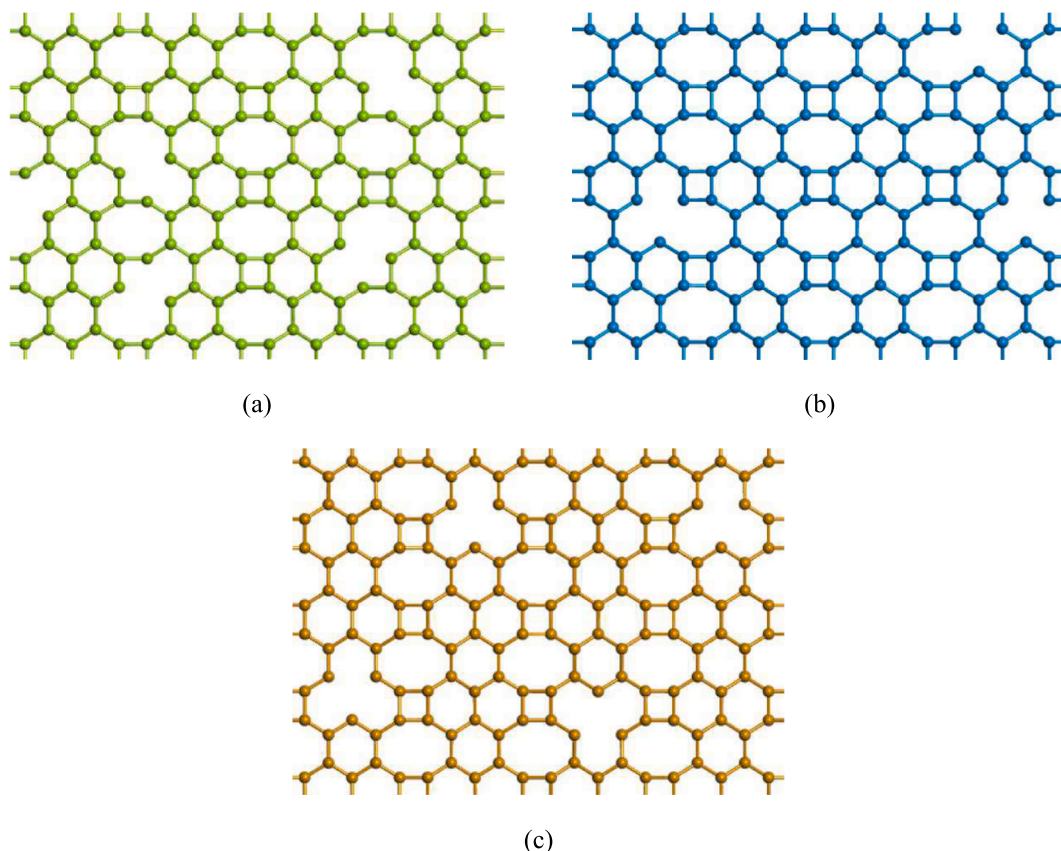


Fig. 21. Distribution of 1.5 % random vacancy defects imposed on each inequivalent carbon atom site: (a) C1; (b) C2; (c) C3.

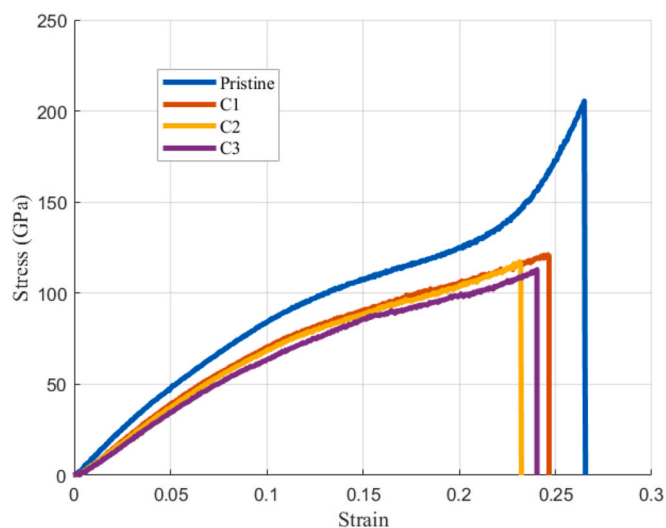


Fig. 22. Stress–strain curves along with X direction for pristine Net Y and for Net Y structures with 1.5 % random vacancy defects at the C1, C2, and C3 sites.

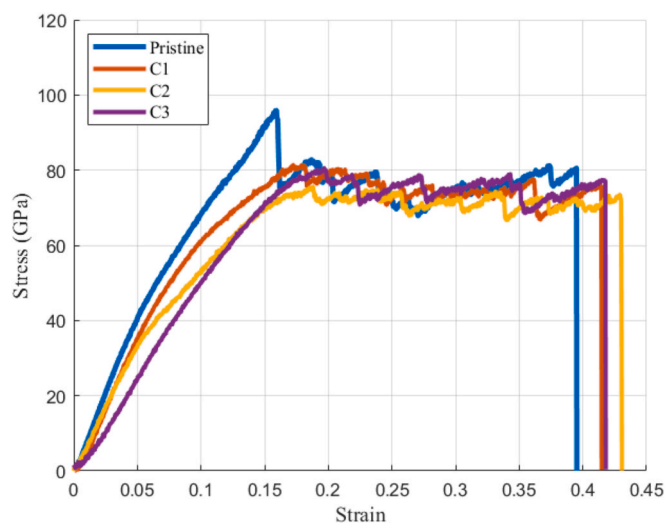


Fig. 23. Stress–strain responses along with Y direction for the pristine Net Y and Net Y structures with 1.5% random vacancies introduced at C1, C2, and C3 atomic sites.

Table 7

Failure stress, failure strain, Young’s modulus, and strain energy values attributed to the pristine structure and for structures with 1.5% vacancies at the introduced C1, C2, and C3 sites.

Defect density %	Failure stress (GPa)	Failure strain	Young’s modulus (GPa)	Strain energy
Pristine	205.5303	0.265	1022	3.622E-25
C1	120.165	0.2650	853.4	2.4521E-25
C2	118.17	0.2320	807.200	2.214E-25
C3	113.68	0.2403	759.1	2.20E-25

found in actual nanosheet materials [49,50].

While a new classification is applied by randomly removing atoms from the inequivalent carbon sites (C1, C2, and C3), the randomness of this process still impacts the outcomes. Even within each category, the unpredictable positioning of defects can lead to variations in the associated mechanical behavior.

Table 8

First failure stress, first failure strain, Young’s modulus, strain energy, ultimate failure stress, and ultimate failure strain values for the pristine structure and for structures with 1.5% vacancies at the introduced C1, C2, and C3 sites.

Defect density %	First fail stress (GPa)	First fail strain	Young’s modulus (GPa)	Strain energy	Ult Fail Stress (GPa)	Ult Fail Strain
Pristine	95.988	0.1589	887.3070	3.43E-25	80.6	0.395
C1	81.230	0.1789	772.2100	3.62E-25	76.7644	0.413
C2	75.43	0.1879	667.61	3.56E-25	73.48	0.429
C3	80.49	0.1966	641.4	3.49E-25	77.34	0.417

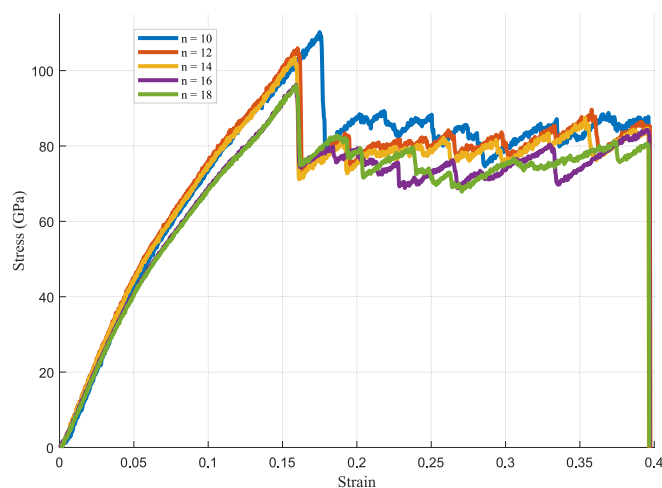


Fig. 24. Stress per strain for ribbons including n = 10, n = 12, n = 14, n = 16, and n = 18 in the X direction investment and applying the tensile loading condition in the Y direction.

3.5. Nanoribbon effect

The nanoribbons are analyzed in two orientations: along with the X axis when a tensile loading condition is imposed along with the Y axis incorporating (‘n’) quantities of 10, 12, 14, 16, and 18, as well as along with the Y axis, when a tensile loading condition is imposed along with the X axis incorporating (‘n’) quantities of 13, 16, 19, 22, and 25. Young’s modulus, failure stress and strain, and tensile toughness are evaluated for both orientations.

Figure 24 displays the stress–strain paths attributed to various (‘n’) quantities in nanoribbons subjected to tensile loading condition along the Y direction (X axis orientation). As (‘n’) increases, both first and ultimate failures occur earlier. This behavior is consistent with the application of tensile loading along with the Y axis for nanoribbons aligned along with the X axis. Figure 25 illustrates the stress–strain paths for nanoribbons along with the Y axis orientation under a tensile loading condition imposed along with the X axis. Similarly, failure occurs earlier as (‘n’) increases. In this configuration, a tensile loading condition is imposed along with the X axis.

Table 9 summarizes the mechanical characters of nanoribbons studied in the X axis orientation, including first failure stress as well as strain, Young’s modulus, and strain energy. Table 10 provides similar characters for nanoribbons in the Y axis orientation.

In Table 9, as (‘n’) enhances along with the X axis orientation, the quantity of Young’s modulus reduces. For example, at (n = 16), Young’s modulus is 890.7GPa. First failure stress and ultimate failure stress also decrease. At (n = 14), these values are 103.41GPa and 84.27GPa,

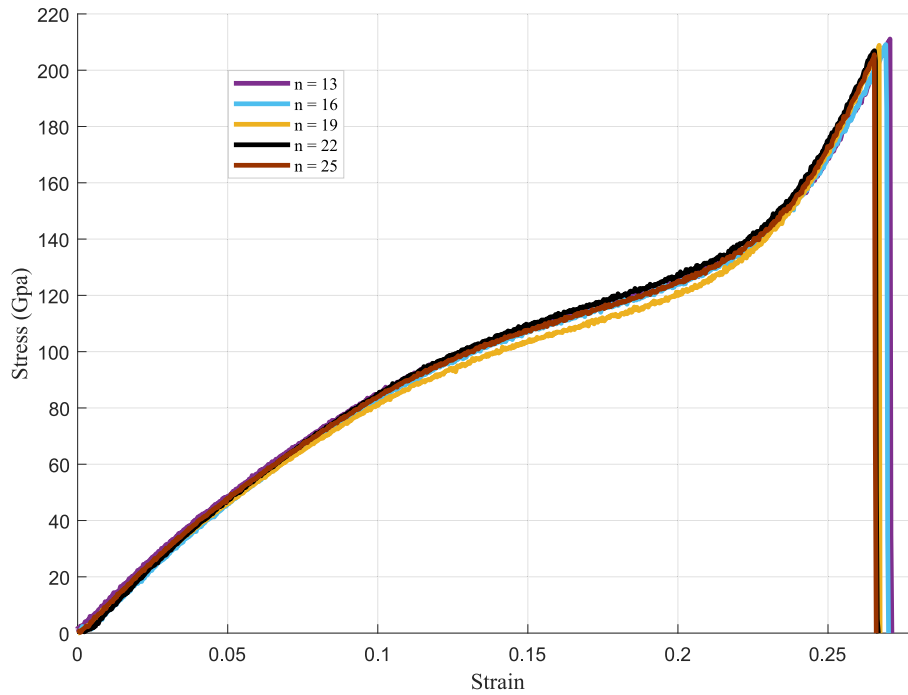


Fig. 25. Stress per strain for ribbons including $n = 13$, $n = 16$, $n = 19$, $n = 22$, and $n = 25$ in the Y direction investment and applying the tensile loading condition in the X direction.

Table 9

The dimensions, Young's modulus, ultimate stress, ultimate strain, and strain energy for nanoribbon investigation including $n = 10$, $n = 12$, $n = 14$, $n = 16$, and $n = 18$ in the Y direction and applying the tensile loading condition in the X direction.

n	First Fail Stress Y (GPa)	First Fail Strain Y	Ult Fail Stress Y (GPa)	Ult Fail Strain Y	Young's Modulus (GPa)	Strain Energy (eV)
10	110.2100	0.1750	87.7400	0.3590	980.52	4.015E-25
12	105.930	0.1600	86.0700	0.3960	972.5	3.93E-25
14	103.415	0.1590	84.2700	0.3960	960.7	3.83E-25
16	96.211	0.1590	84.2100	0.3950	890.7	3.622E-25
18	95.988	0.1590	80.6000	0.3950	887.3	3.622E-25

Table 10

The dimensions, Young's modulus, failure stress, failure strain, and strain energy for nanoribbon investigation including $n = 13$, $n = 16$, $n = 16$, $n = 22$, and $n = 25$ in the Y direction and applying the tensile loading condition in the X direction.

n	Failure stress (GPa)	Failure Strain	Young's Modulus (GPa)	Strain energy (eV)
13	211.09	0.2707	978.85	3.593E-25
16	209.130	0.2692	1000.000	3.50E-25
19	208.850	0.2671	1002.000	3.49E-25
22	206.930	0.2655	1018.000	3.48E-25
25	205.5303	0.2654	1022.000	3.43E-25

respectively, while for ($n = 16$), they are 96.21GPa and 84.21GPa. The first failure strain and ultimate failure strain show a slight decrease, with values of 0.16 for ($n = 12$), and 0.159 for ($n = 16$). Strain energy declines with increasing (n '), with values of 3.83×10^{-25} eV and 3.622×10^{-25} eV, respectively.

In Table 10, for the nanoribbons along with the Y axis orientation,

ultimate failure stress reduces slightly as (n '), enhances. For example, the stress at ($n = 13$), is 211.9GPa, and the difference in failure stress between ($n = 13$), and ($n = 25$), is 5.55GPa. Failure strain also decreases slightly, with a difference of 0.0053 between ($n = 13$), and ($n = 25$). In contrast to the X axis orientation, Young's modulus increases with (n '); at ($n = 16$), Young's modulus reaches 1000GPa. Strain energy declines rapidly as (n '), increases. For instance, at ($n = 13$), the strain energy is 3.59×10^{-25} eV and 3.43×10^{-25} eV, respectively.

4. Conclusion

This study used molecular dynamics simulations to investigate the mechanical properties of Net Y under varying defect densities and temperature gradients. Key parameters such as Young's modulus, strain energy, failure stress, and failure strain were analyzed under tensile stress applied along the X and Y directions.

The results revealed that the defect density, as well as the temperature gradients, significantly affect the mechanical performance of Net Y. In this regard, as the temperature gradients increase, the allocated mechanical properties further decline. The values for failure stress and failure strain along the X direction, first failure stress as well as first failure strain, ultimate failure stress, and ultimate failure strain for the Y direction were equal to 205.53GPa, 0.265, 95.988GPa, 0.159, 80.60GPa, and 0.395, respectively. Moreover, the strain energy decreases via increasing the temperature, as the X direction experiences a sharper decline compared to the Y direction. For instance, the strain energy drops from 3.43×10^{-25} eV to 2.1×10^{-25} eV as the temperature rises along with the X axis.

Furthermore, it was found that increasing the defect density reduces the failure stress as well as the strain along the X direction, besides the first failure and ultimate failure stress along the Y direction, while minimally increasing the first and ultimate failure strain due to vacancies and porosity imposed on the nanosheet during Y direction tensile displacement. Additionally, Young's modulus consistently declines with higher defect densities, dropping from 963.65 GPa at 0.5 % defect density to 791 GPa at 2 % defect density in the X direction.

On the contrary, for nanoribbons, enhancing the (n ') quantities

leads to earlier failure and reduced mechanical performance along with the X axis, when a tensile stress is imposed along with the Y axis. Conversely, along with the Y axis, the quantity of Young's modulus increases with ('n'), although failure stress and strain show only minor changes.

CRedit authorship contribution statement

Mohsen Eghbalian: Investigation, Formal analysis, Conceptualization. **Mohammad Javad Hashemi:** Investigation, Formal analysis, Conceptualization. **Amirhossein Nikparsa:** Writing – original draft, Investigation, Formal analysis. **Reza Ansari:** Supervision, Project administration, Methodology, Conceptualization. **Saeid Sahmani:** Validation, Methodology, Data curation, Conceptualization. **Eligiusz Postek:** Writing – review & editing, Software, Resources, Conceptualization.

Declaration of competing interest

The authors declare that they have no known competing financial interests or personal relationships that could have appeared to influence the work reported in this paper.

Acknowledgement

This paper was supported by statutory funding of the Institute of Fundamental Technological Research Polish Academy of Sciences.

Appendix A. Supplementary material

Supplementary data to this article can be found online at <https://doi.org/10.1016/j.commatsci.2025.114049>.

Data availability

Data will be made available on request.

References

- [1] L. Shen, H.-S. Shen, C.-L. Zhang, Nonlocal plate model for nonlinear vibration of single layer graphene sheets in thermal environment, *Comput. Mater. Sci* 48 (2010) 680–685.
- [2] R. Ansari, S. Sahmani, B. Arash, Nonlocal plate model for free vibrations of single-layered graphene sheets, *Phys. Lett. A* 375 (2010) 53–62.
- [3] A. Bianco, H.-M. Cheng, T. Enoki, Y. Gogotsi, R.H. Hurt, N. Koratkar, et al., All in the graphene family—a recommended nomenclature for two-dimensional carbon materials, *Carbon* 65 (2013) 1–6.
- [4] R. Nandee, M.A. Chowdhury, M.M. Rana, N. Hossain, M.A. Islam, H. Aoyon, Analysis of semiconductor properties of fabricated graphene materials, *Nano-Struct. Nano-Objects* 40 (2024) 101334.
- [5] A. Nikparsa, R. Ansari, M. Eghbalian, Characterization of the mechanical properties of N-triphenylene nanosheet under atomistic defect and thermal gradient by molecular dynamics simulations, *The European Physical Journal plus* 140 (2025) 1–19.
- [6] Y. Xu, P. Zhou, T. Simon, T. Cui, Dual-function graphene sensor as an ion-sensitive field-effect transistor and ion-sensitive electrode for arsenite detection, *Carbon* 242 (2025) 120419.
- [7] S.K. Yadav, A. Kumar, N. Mehta, Beyond graphene basics: a holistic review of electronic structure, synthesis strategies, properties, and graphene-based electrode materials for supercapacitor applications, *Prog. Solid State Chem.* 78 (2025) 100519.
- [8] Y. Xia, W. Gao, C. Gao, A review on graphene-based electromagnetic functional materials: electromagnetic wave shielding and absorption, *Adv. Funct. Mater.* 32 (2022) 2204591.
- [9] R. Matsuoka, R. Toyoda, R. Shiotsuki, N. Fukui, K. Wada, H. Maeda, et al., Expansion of the graphdiyne family: a triphenylene-cored analogue, *ACS Appl. Mater. Interfaces* 11 (2018) 2730–2733.
- [10] V.N. Popov, Carbon nanotubes: properties and application, *Mater. Sci. Eng. R. Rep.* 43 (2004) 61–102.
- [11] R. Ansari, S. Sahmani, Prediction of biaxial buckling behavior of single-layered graphene sheets based on nonlocal plate models and molecular dynamics simulations, *App. Math. Model.* 37 (2013) 7338–7351.

- [12] A.H.N. Shirazi, R. Abadi, M. Izadifar, N. Alajlan, T. Rabczuk, Mechanical responses of pristine and defective C3N nanosheets studied by molecular dynamics simulations, *Comput. Mater. Sci* 147 (2018) 316–321.
- [13] S. Sun, G. Ru, W. Qi, W. Liu, Molecular dynamics study of the robust superlubricity in penta-graphene van der Waals layered structures, *Tribol. Int.* 177 (2023) 107988.
- [14] M. Eghbalian, R. Ansari, S. Haghighi, Elastic properties of randomly dispersed functionalized silicon carbide nanotubes/polymer nanocomposites: combined multiscale molecular dynamics and finite element modeling, *SILICON* 15 (2023) 4795–4809.
- [15] W. Yang, L. Tang, Y. Liu, X. Wang, Y. Luo, H. Zhang, D. Mao, Effect of hydrogen concentration on the friction evolution mechanism of few-layer graphene: a molecular dynamics study in nanoscratch processes, *Surf. Sci.* 740 (2024) 122414.
- [16] N. Kametani, M. Nakamura, K. Yashiro, T. Takaki, Impact of temperature on residual stress and bonding in diamond-like carbon film: a molecular dynamics study under various deposition conditions, *Comput. Mater. Sci* 238 (2024) 112950.
- [17] A. Fukuhima, H. Uematsu, Interfacial adhesion of polycarbonate to graphene and silicon oxide: a comparative molecular dynamics analysis, *Surf. Interfaces* 55 (2024) 105323.
- [18] K. Jiang, J. Wang, J. Yuan, Q. Wang, Investigating vacancy-defect effects on the vibration characteristics of graphene resonators with molecular dynamics simulation, *Comput. Mater. Sci* 252 (2025) 113794.
- [19] G. Zhu, Q. Liu, Z. Liu, J. Xu, Molecular dynamics simulation study on the adsorption characteristics and microstructures of pyridinium ionic liquids on the surface of carbon nanotubes, *J. Mol. Liq.* 432 (2025) 127733.
- [20] X. Gao, H. Liu, D. Wang, J. Zhang, Graphdiyne: synthesis, properties, and applications, *Chem. Soc. Rev.* 48 (2019) 908–936.
- [21] Y. Li, L. Xu, H. Liu, Y. Li, Graphdiyne and graphyne: from theoretical predictions to practical construction, *Chem. Soc. Rev.* 43 (2014) 2572–2586.
- [22] M.F.L. De Volder, S.H. Tawfik, R.H. Baughman, A.J. Hart, Carbon nanotubes: present and future commercial applications, *Science* 339 (2013) 535–539.
- [23] K. Khan, A.K. Tareen, M. Iqbal, Z. Shi, H. Zhang, Z. Guo, Novel emerging graphdiyne based two dimensional materials: synthesis, properties and renewable energy applications, *Nano Today* 39 (2021) 101207.
- [24] C. Huang, Y. Li, N. Wang, Y. Xue, Z. Zuo, H. Liu, Y. Li, Progress in research into 2D graphdiyne-based materials, *Chemical Review* 118 (2018) 7744–7803.
- [25] B. Mortazavi, M. Shahrokhi, M.E. Madjet, M. Makaremi, S. Ahzi, T. Rabczuk, N-, P-, As-triphenylene-graphdiyne: strong and stable 2D semiconductors with outstanding capacities as anodes for Li-ion batteries, *Carbon* 141 (2019) 291–303.
- [26] Q. Peng, A. Dearden, J. Crean, L. Han, S. Liu, X. Wen, S. De. New materials graphyne, graphdiyne, graphone, and graphane: review of properties, synthesis, and application in nanotechnology. *Nanotechnol. Sci. Appl.*, pp. 1–29, 2014.
- [27] M. Eghbalian, R. Ansari, M.O. Bidgoli, S. Rouhi, Finite element investigation of the geometrical parameters of waviness carbon nanotube on directional young's and shear elastic modulus of polymer nanocomposites, *J. Inst. Eng. (India): Series D* 104 (2023) 609–622.
- [28] W.C. Lothrop, Biphenylene, *J. Am. Chem. Soc.* 63 (1941) 1187–1191.
- [29] Q. Fan, L. Yan, M.W. Tripp, O. Krejci, S. Dimosthenous, S.R. Kachel, et al., Biphenylene network: a nonbenzenoid carbon allotrope, *Science* 372 (2021) 852–856.
- [30] X.-Q. Wang, H.-D. Li, J.-T. Wang, Prediction of a new two-dimensional metallic carbon allotrope, *PCCP* 15 (2013) 2024–2030.
- [31] M.A. Hudspeth, B.W. Whitman, V. Barone, J.E. Peralta, Electronic properties of the biphenylene sheet and its one-dimensional derivatives, *ACS Nano* 4 (2010) 4565–4570.
- [32] N.N. Karaush, G.V. Baryshnikov, B.F. Minaev, DFT characterization of a new possible graphene allotrope, *Chem. Phys. Lett.* 612 (2014) 229–233.
- [33] S. Yu, Y.-C. Rao, S.-F. Li, X.-M. Duan, Net W monolayer: a high-performance electrode material for Li-ion batteries, *Appl. Phys. Lett.* 112 (2018) 053903.
- [34] A. Hamzei, H. Hajiabadi, M.T. Rad, Wettability of net C, net W and net Y: a molecular dynamics simulation study, *RSC Adv.* 13 (2023) 2318–2328.
- [35] J. Rong, H. Dong, J. Feng, X. Wang, Y. Zhang, X. Yu, Z. Zhan, Planar metallic carbon allotrope from graphene-like nanoribbons, *Carbon* 135 (2018) 21–28.
- [36] S. Plimpton, Fast parallel algorithms for short-range molecular dynamics, *J. Comput. Phys.* 117 (1995) 1–19.
- [37] A.P. Thompson, H.M. Aktulga, R. Berger, D.S. Bolintineanu, W.M. Brown, P. S. Crozier, et al., LAMMPS – a flexible simulation tool for particle-based materials modeling at the atomic, meso, and continuum scales, *Comput. Phys. Commun.* 271 (2022) 108171.
- [38] S.J. Sturat, A.B. Tutein, J.A. Harrison, A reactive potential for hydrocarbons with intermolecular interactions, *J. Chem. Phys.* 112 (2000) 6472–6486.
- [39] <https://www.3ds.com/products/biovia/materials-studio>.
- [40] L. Pauling, The nature of the chemical bond and the structure of molecules and crystals: an introduction to modern structural chemistry, Cornell University Press, 1960.
- [41] M.P. Allen, D.J. Tildesley, Computer simulation of liquids, Oxford University Press, 2017.
- [42] R. Ansari, S. Rouhi, M. Eghbalian, On the elastic properties of curved carbon nanotubes/polymer nanocomposites: a modified rule of mixture, *J. Reinf. Plast. Compos.* 36 (2017) 991–1008.
- [43] R. Ansari, B. Motevalli, A. Montazeri, S. Ajori, Fracture analysis of monolayer graphene sheets with double vacancy defects via MD simulation, *Solid State Commun.* 151 (2011) 1141–1146.
- [44] J.-W. Jiang, J.-S. Wang, B. Li, Young's modulus of graphene: a molecular dynamics study, *Phys. Rev. B* 80 (2009) 113405.

- [45] M. Mirnezhad, M. Modarresi, R. Ansari, M.R. Roknabadi, Effect of temperature on young's modulus of graphene, *J. Therm. Stresses* 35 (2012) 913–920.
- [46] S. Zhang, J. Zhou, Q. Wang, X. Chen, Y. Kawazoe, P. Jena, Penta-graphene: a new carbon allotrope, *Proc. Natl. Acad. Sci.* 112 (2015) 2372–2377.
- [47] H. Zhao, N.R. Aluru, Temperature and strain-rate dependent fracture strength of graphene, *J. Appl. Phys.* 108 (2010) 064321.
- [48] Y.Y. Zhang, Y.T. Gu, Mechanical properties of graphene: effects of layer number, temperature and isotope, *Comput. Mater. Sci* 71 (2013) 197–200.
- [49] J.C. Meyer, A.K. Geim, M.I. Katsnelson, K.S. Novoselov, T.J. Booth, S. Roth, The structure of suspended graphene sheets, *Nature* 446 (2007) 60–63.
- [50] F. Banhart, J. Kotakoski, A.V. Krasheninnikov, Structural defects in graphene, *ASC Nano* 5 (2011) 26–41.